San Jose State University

SJSU ScholarWorks

Faculty Research, Scholarly, and Creative Activity

10-11-2021

Improved shadow correction for the marine optical buoy, MOBY

Kenneth Voss
University of Miami

Edouard Leymarie
Sorbonne Université

Stephanie Flora
San Jose State University, stephanie.flora@sjsu.edu

B. Carol Johnson
National Institute of Standards and Technology

Arthur Gleason
University of Miami

See next page for additional authors

Follow this and additional works at: https://scholarworks.sjsu.edu/faculty_rsca

Recommended Citation

Authors

Kenneth Voss, Edouard Leymarie, Stephanie Flora, B. Carol Johnson, Arthur Gleason, Mark Yarbrough, Michael Feinholz, and Terrance Houlihan

Improved shadow correction for the marine optical buoy, MOBY

KENNETH VOSS,[1,*] ᴵᴰ EDOUARD LEYMARIE,[2] ᴵᴰ STEPHANIE FLORA,[3] B. CAROL JOHNSON,[4] ᴵᴰ ARTHUR GLEASON,[1] MARK YARBROUGH,[3] MICHAEL FEINHOLZ,[3] AND TERRANCE HOULIHAN[3]

[1]*Physics Department, University of Miami, Coral Gables, Fl. 33124, USA*
[2]*Laboratoire d'Océanographie de Villefranche, CNRS, Sorbonne Université, Villefranche-sur-Mer, France*
[3]*Moss Landing Marine Laboratories, San Jose State University, Moss Landing, CA 95039, USA*
[4]*Sensor Science Division, National Institute of Standards and Technology, Gaithersburg, MD 20899, USA*
*kvoss@miami.edu

Abstract: A 3-D instrument self-shading correction has been developed for the MOBY upwelling radiance measurements. This correction was tested using the 23 year time series of MOBY measurements, at the Lanai, Hawaii site. The correction is small (less than 2%) except when the sun and collectors are aligned within 20° azimuth on opposite sides of the main MOBY structure. Estimates of the correction uncertainty were made with a Monte-Carlo method and the variation of the model input parameters at this site. The correction uncertainty was generally less than 1%, but increased to 30% of the correction in the strongest shadow region.

1. Introduction

Any optical instrument, placed in the water to measure the light field, will perturb the light field to some extent in a process called instrument self-shading (ISS) [1]. Several instruments and platforms have been modeled in detail in order to assess and/or correct for ISS, usually through a Monte-Carlo radiative transfer model (e.g. [2–5]). The Marine Optical BuoY (MOBY) ISS was previously modeled as a two-dimensional (2-D) problem [6], but in this paper we present an improved shadowing correction using the SimulO program (https://lov.imev-mer.fr/web/project/simulo/) with a more realistic three dimensional (3-D) model of the instrument. SimulO [7] is a 3-D backwards Monte-Carlo radiative transfer model which allows a realistic model of the structure above and below the water surface to be implemented. SimulO has been used to model the ISS for other in-situ instruments [8,9]. It uses a realistic skylight distribution, and allows the optical properties of the water to be specified. It can run on several operating systems; we performed these calculations on a Linux cluster.

MOBY is an instrumented spar buoy that has been used off of Lanai, Hawaii since 1997 [10,11]. The system collects downwelling irradiance above the surface (Es), downwelling irradiance at 3 fixed depths (Ed(1 m), Ed(5 m), and Ed(9 m)), and upwelling radiance at 3 depths (Lu(1 m), Lu(5 m), and Lu(9 m)). The in-water collectors are at the end of arms which extend 3 m, 2.5 m, and 2 m from the central buoy at 1 m, 5 m, and 9 m, respectively. Each collector, radiance and irradiance, is coupled to a fiber optic, which transmits the light from the collector to a spectrometer at the bottom of the buoy. The spectrometer measures the signal from each collector sequentially, and the respective light measurement from 380 nm to 900 nm at 1 nm resolution is determined. Clark et al. [11] described the optical measurements and buoy in detail. Measurement sets are collected at three fixed times each day, with times determined by the satellite programs being supported. MOBY data are used for vicarious calibration of many NASA (National Aeronautics and Space Administration)**,** NOAA (National Oceanic and Atmospheric Administration), and international satellite programs [12–14]. Data are openly available at the NOAA Coastwatch site (https://coastwatch.noaa.gov/cw/field-observations/MOBY.html).

This paper will describe the results of using the SimulO program to determine the shadowing correction needed for the MOBY water leaving radiance data set, and then test this correction on our historical data set. In addition we will estimate the uncertainty of this correction, based on the uncertainty of the inputs to the SimulO program.

2. Methods

MOBY was modeled in the SimulO program as shown in Fig. 1. The model consists of several stacked cylinders, some above the water, some below, along with the three arms sticking out from the central buoy.
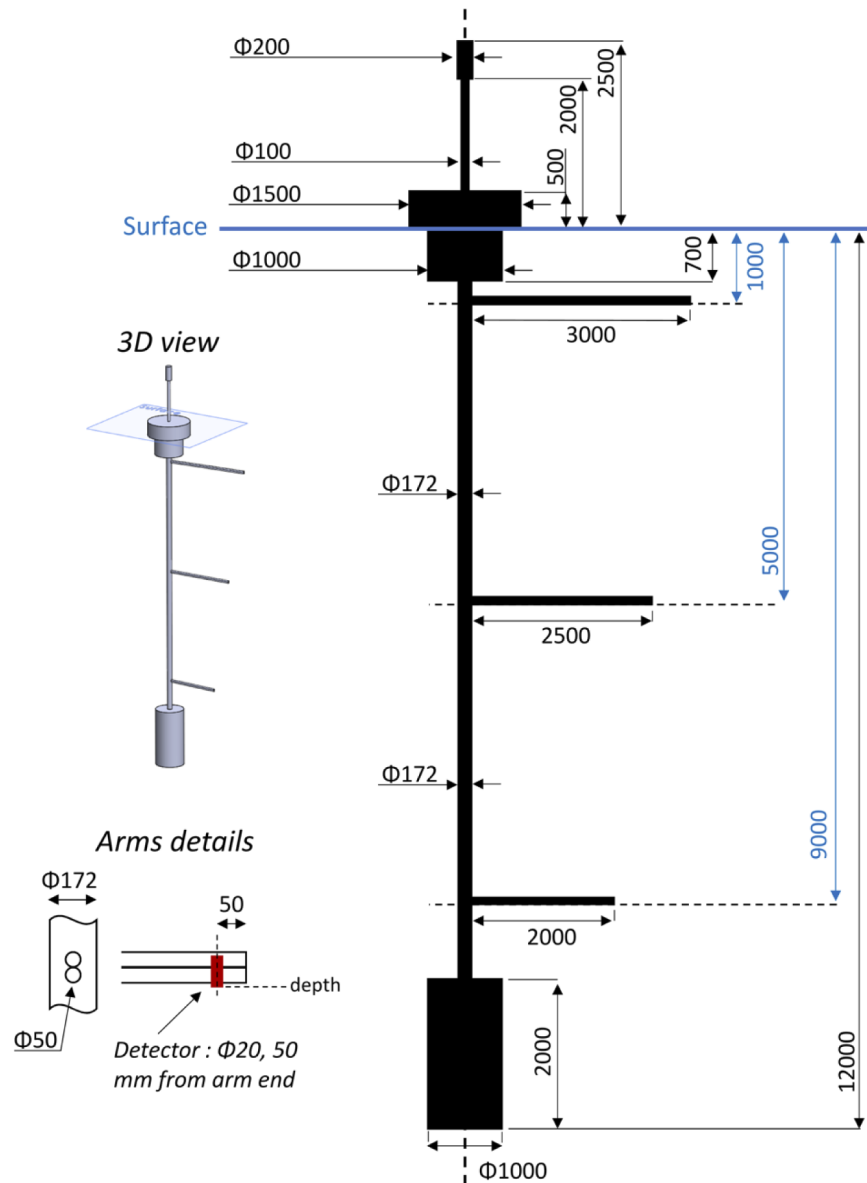

Fig. 1. Diagram of MOBY as included in 3-D model for SimulO. All dimensions are in millimeters.

The full angle acceptance of the radiance collectors in MOBY is 0.5°, however MOBY is not a fixed platform and moves slightly during the measurement period. The typical integration time for the upwelling measurements is 30 s to 1 min. Statistically there is a 2° variation in the pointing of MOBY around the average measurement direction during this integration time. Thus while the acceptance angle at any one moment is 0.5°, during the measurement MOBY is sampling a much larger range of angles. To account for this, the acceptance angle of the radiance detectors in the SimulO runs were opened up to 2°.

Simulations were run for wavelengths at 350 nm and then 360 nm to 700 nm at 20 nm increments. The relative azimuth angle, φ, is the angle between the solar azimuth and the direction the MOBY arm is pointing, with 0° representing the collector end of the arm pointing towards the sun. Results were binned for φ from 1.5° to 178.5° in 3° increments, and solar zenith angles, θ_o, from 0.5° to 59.5° in 1° increments. The upper limit of 59.5° for θ_o is slightly larger than the maximum solar zenith angle at which we collect data. Simulations were performed with the instrument in place, then with the instrument removed, to allow the difference, the ISS, to be determined. The output data are convolved with a model of the spectral radiance of a blue sky. The blue sky diffuse light field is modeled by using Harrison [15] for which the parameters C (opaque cloud cover) is always taken at zero. Therefore, this diffuse light field depends only on the Sun's elevation. On top of the diffuse light field, a direct solar radiance is added. The ratio between direct and diffuse radiance is provided by [16] depending on the position, wavelength and solar elevation. The program provides the fraction of $Lu(z)$ which has been shadowed for each θ_o and φ.

Ten sets of calculations were done for each arm depth. In each set, the calculation was run 200 times, with each run using 2.5×10^8 photons. We used the set of 10 calculations to estimate the residual statistical noise in the calculations. The pure water optical properties were taken from Pope and Fry [17] and Morel [18]. Figure 2 shows the optical properties of the water constituents assumed in the base model. The particulate phase function was assumed to be a Fournier-Forand phase function [19]. Using the MOBY hyperspectral data, the CI -Chlorophyll algorithm [20] can be used to determine a first order estimate for the Chlorophyll (*Chl*) at the site. For the 23 year time series, the average *Chl* is 0.08 mg/m^3, with a standard deviation of 0.007 mg/m^3. For the base calculation *Chl* was used as an index of water type with the particulate absorption, a_p, and scattering, b_p, derived with *Chl*=0.1 mg/m^3 and the model of Morel and Maritorena [21]. These optical properties are shown in Fig. 2. For the Fournier-Forand particle phase function, the ratio of particulate backscattering (b_{bp}) to particulate scattering (b_p) was assumed to be 0.0183, following Petzold [22]. In all cases the optical properties were assumed to be constant with depth. A useful term, to quantify the relative importance of scattering and absorption is the single scattering albedo, $a/(a + b)$. These calculations were done for the upwelling radiance collectors on each arm. The uncertainties involved with variation of these parameters will be discussed below.

The main product obtained from the MOBY measurement is the water leaving radiance. This is calculated as:

$$LwX = \frac{1 - \rho}{n^2} Lu(z_1) e^{K_L z_1}, \qquad (1)$$

ρ is the Fresnel reflectance of the sea surface, n is the water index of refraction, $Lu(z_1)$ is the upwelling radiance, at depth z_1, and K_L is the upwelling radiance diffuse attenuation coefficient, calculated with a pair of upwelling radiance measurements. LwX represents one of three water leaving radiance products that are produced with the 3 upwelling radiance measurements. *Lw1* uses $Lu(1 \text{ m})$ and calculates K_L between 1 m and 5 m, *Lw2* uses $Lu(1 \text{ m})$ and calculates K_L between 1 m and 9 m, and *Lw7* uses $Lu(5 \text{ m})$ and calculates K_L between 5 m and 9 m, where K_L
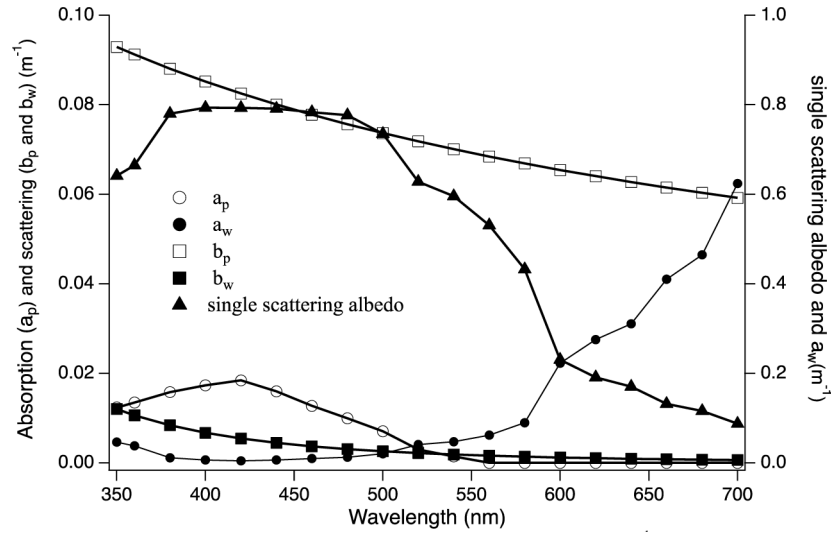
Fig. 2. Optical properties used in base radiative transfer model. Absorption, a (m^{-1}), and scattering, b (m^{-1}), were determined using the Morel and Maritorena [21] and assuming Chl=0.1 mg/m^3 . Pure water values (a_w and b_w) were from [17,18].

is given by:

$$K_L = -\frac{ln\left(\frac{Lu(z_2)}{Lu(z_1)}\right)}{(z_2 - z_1)} \quad . \tag{2}$$

In this equation z_2 is the deeper of the measurement depths.

Shadowing can introduce errors in both $Lu(z)$ and in the calculation of K_L, through its effect on Lu at the two arm depths. The true $Lu(z)$, $LuT(z)$, and the measured $Lu(z)$, $LuM(z)$, can be connected via the shadowing factor:

$$LuM(z) = LuT(z)F(\theta_o, \varphi, z) \quad . \tag{3}$$

where $F(\theta_o, \varphi, z)$ is the shadow factor calculated with SimulO for a specific θ_o and φ. Note $F(\theta_o, \varphi, z)$ also depends on the water properties (a and b), but this is not explicitly included in the notation. Taking into account the effect of shadowing on both $Lu(z_1)$ and $Lu(z_2)$ one obtains:

$$LwX = \frac{LuM(z_1)}{F(\theta_o, \varphi, z_1)} e^{-\frac{ln([LuM(z_2)/F(\theta_o,\varphi,z_2)]/[LuM(z_1)/F(\theta_o,\varphi,z_1)])}{(z_2-z_1)}z_1}, \tag{4}$$

or

$$LwX = LwXM * \frac{e^{-\frac{ln\left(\frac{[F(\theta_o,\varphi,z_1)]}{[F(\theta_o,\varphi,z_2)]}\right)}{(z_2-z_1)}z_1}}{F(\theta_o, \varphi, z_1)} = LwXM * \frac{\frac{[F(\theta_o,\varphi,z_1)]}{[F(\theta_o,\varphi,z_2)]}^{\frac{z_1}{z_1-z_2}}}{F(\theta_o, \varphi, z_1)} = LwXM * S(\theta_o, \varphi). \tag{5}$$

Here $LwXM$ is LwX calculated with the measured Lu at z_1 and z_2, and $S(\theta_o, \varphi)$ is the total shadowing correction needed for the specific measured LwX. $LwnX$ is the normalized water leaving radiance, which is simply LwX divided by the measured solar irradiance and multiplied by the extra-terrestrial solar irradiance at the average sun and the earth distance. [23]

With a smooth surface, the edges of the shadow can be sharply defined near the surface, where scattering has not significantly modified the light field. While not a large effect in the upwelling radiance, we developed a method to allow the flat surface results to be extended to a rough surface. We used the Monte-Carlo technique to refract light through a rough surface, with the surface

statistics given by an isotropic Cox-Munk distribution [24,25]. We ran cases with windspeeds, W, of 1 m/s, 5 m/s, and 10 m/s and θ_o equal to 15°, 30°, 45°, 60°, and 75°. In each case 10^7 photons were followed and the incoming light rays, $\zeta(\theta_o, 0, W)$, result in a distribution, $N(\theta_o{}', \Delta\varphi', W)$ of subsurface rays, $\zeta'(\theta_o{}', \Delta\varphi', W)$. $\theta_o{}'$ is the subsurface zenith angle, while $\Delta\varphi'$ is the deviation in azimuth between the incoming beam and the subsurface beam. The distribution of subsurface rays are then refracted back through the surface, into the air, assuming a flat surface:

$$N(\theta_o', \Delta\varphi', W) \rightarrow N(\theta_o{}'', \Delta\varphi', W), \tag{6}$$

and the distribution was normalized:

$$\sum N(\theta_o'', \Delta\varphi', W) = 1. \tag{7}$$

The shadow factor, S', for a given θ_o, φ, and W was calculated, using the distribution as a weight and interpolating the original shadow factor, S, to θ_o'' and φ':

$$S'(\theta_o, \varphi, W) = \sum S(\theta_o'', \varphi')N(\theta_o'', \Delta\varphi', W) \tag{8}$$

As will be discussed below, we calculated the $S'(\theta_o, \varphi, W)$ using the single value of 5 m/s windspeed and used the other windspeeds to estimate the uncertainty in this assumption.

The MOBY data set provides a 23 year time series that can be used to validate the shadow correction. To test the shadow correction factor, $S'(\theta_o, \varphi, W)$, we binned the data set by θ_o and φ. We focused on the normalized water leaving radiance, Lwn, to reduce variability due to illumination conditions. Ignoring polarization sensitivity, which is a small factor in MOBY, $S'(\theta_o, \varphi, W)$ should be the major cause of an asymmetry of Lwn with φ. We will also concentrate on $Lwn1$, which is the product with the smallest uncertainty, as it requires a smaller factor to propagate $Lu(1\text{ m})$ to the surface as opposed to $Lu(5\text{ m})$, and also derives the K_L from the two Lu values closest to the surface. We will focus on 2 wavelength bands, integrated over channels of the Visible and Infrared Imager/Radiometer Suite (VIIRS) satellite sensor [26], 444.5 nm (or rounded to 440 nm in results) and 556.3 nm (or rounded to 560 nm in results) using the VIIRS instrument's spectral response function. The first, 444.5 nm, represents a low pure water absorption and relatively high single scattering albedo situation. The second, 556.3 nm, represents a higher pure water absorption and lower single scattering albedo situation but still below the spectral region of strong inelastic scattering influence, which starts at 575 nm [27,28].

3. Results

The magnitude and shape of the ISS correction, $S'(\theta_o, \varphi, W = 5\text{ }m/s)$, are shown in Fig. 3 for 440 and 560 nm, as a function of θ_o and φ for $Chl = 0.1\text{ mg/m}^3$ (optical properties given in Fig. 2). The reference frame for φ is 0° when the MOBY arm is pointing towards the sun, and 180° when the collection optics are on the opposite side of the MOBY buoy from the sun (worst case for shadowing). The major features are two areas of increased shadow. The largest shadow occurs at $\varphi = 180°$, and at larger θ_o (40° to 50°). Here, along with the in-water structure, the above water MOBY structure is shadowing the portion of water viewed by the upwelling collector. The other place where the shadow increases is near $\theta_o = 0$, when the arm and collector itself becomes important. Shadowing in the blue, other than at $\varphi > 150°$, is less than 5%. At 560 nm, however, the shadowing is approximately double the shadow at 440 nm for many geometries.

To validate the model we used the existing MOBY time series. Our MOBY measurement is within a few degrees of nadir, so without shadowing there should be no significant φ dependence in the time series. There will be a variation in Lwn with θ_o, referred to as the Bi-Directional Reflectance Distribution Function (BRDF) or the f/Q factor [29,30]. $Lwn1$ for two wavelength bands, 444.5 nm and 556.3 nm, shows a large variation with solar zenith angle at all azimuth angles (Fig. 4).
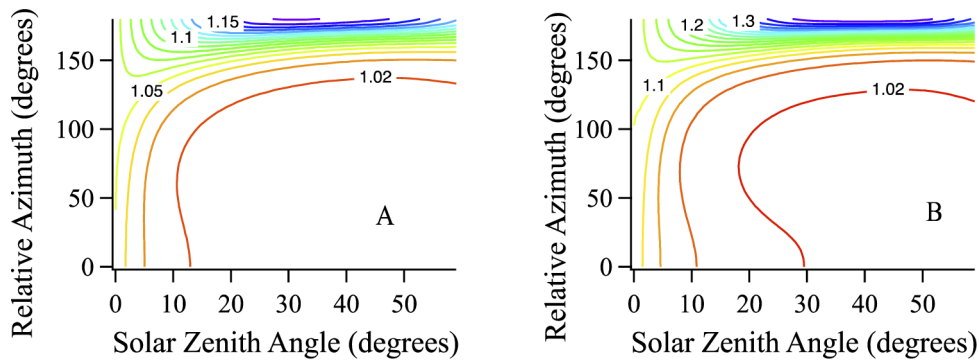
Fig. 3. Example $S'(\theta_o, \varphi, W)$ for Chl=0.1 mg/m^3, $b_b/b = 0.183$, $W = 5$ m/s. A) 440 nm, B) 560 nm. Increased absorption at 560 nm leads to an almost doubling of $S'(\theta_o, \varphi, W)$.
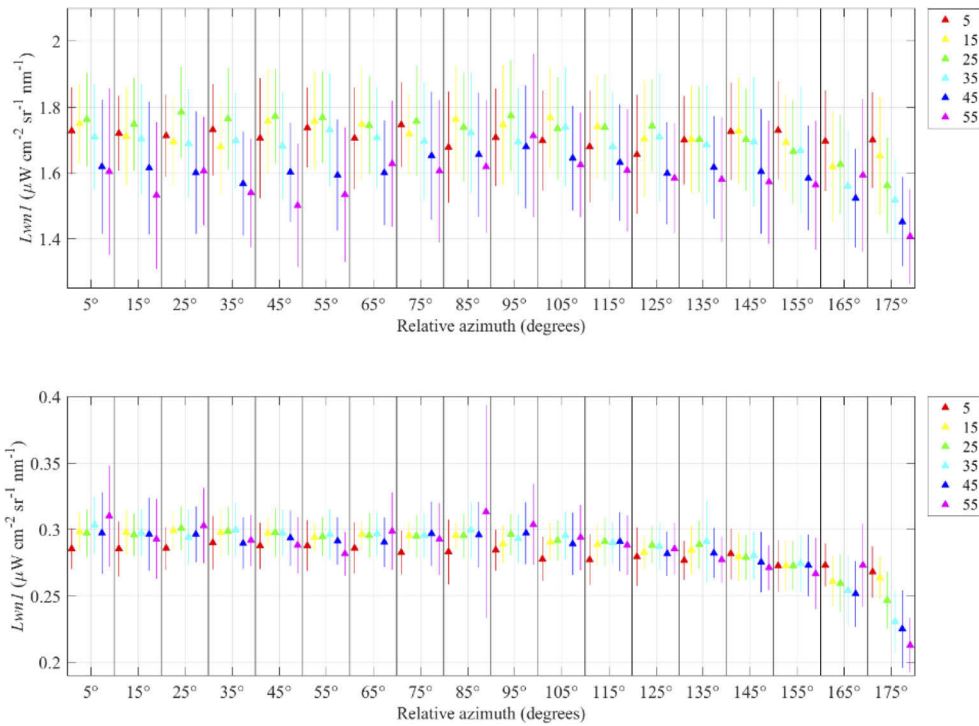

Fig. 4. $Lwn1$ before any corrections for two sample wavelengths, top graph is 444.5 nm and bottom graph is 556.3 nm. The data are binned by solar zenith angles (shown in different colored symbols) and the azimuthal direction of the arm, relative to the sun (along the x axis). On the x-axis, the label represents the center of the 10° bin.

If there were no shadowing from the MOBY structure, one would not expect a variation with azimuthal direction, hence each panel azimuthal group would appear the same. There could be slight variations due to slightly different water properties, statistically showing up in different azimuth bins. To take out some of the known variation with solar zenith angle, we applied the correction described in [30], hereafter after abbreviated MAG2002BRDF, to the Lwn data from the MOBY time series, then binned the data in 10° increments of θ_o and φ. The number of samples in each bin varied a little by φ, but varied strongly with θ_o. In the different bins of θ_o,

the number of samples in each azimuth range was approximately 50, 30, 130, 100, 100, and 20 for zenith angle bins from 0° to 10°, 10° to 20°, 20° to 30°, 30° to 40°, 40° to 50°, and 50° to 60° respectively. In Fig. 5 we show the MAG2002BRDF corrected *Lwn1* for the two wavelength bands, 444.5 nm and 556.3 nm.
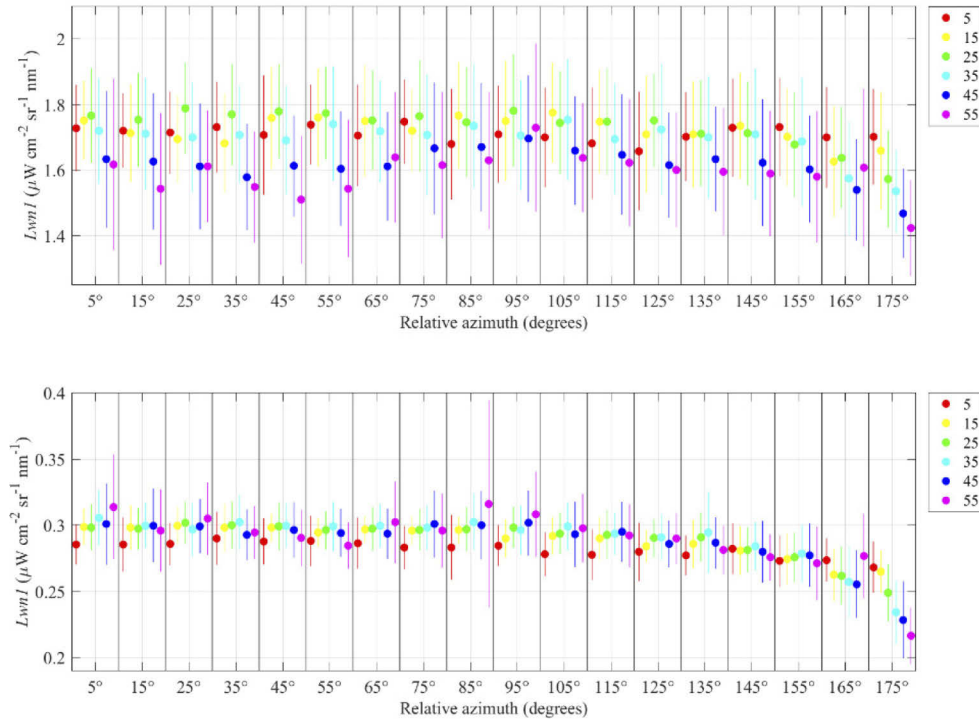

Fig. 5. MOBY time series of *Lwn1* after being corrected for the BRDF effect by MAG2002BRDF and then binned in 10° increments of θ_o and φ. Top graph is 444.5 nm and bottom graph is 556.3 nm. On the x-axis, the label represents the center of the 10° bin.

For 444.5 nm, differences in *Lwn1* as a function of solar zenith angle remained even after the MAG2002BRDF correction (Fig. 5). For φ less than 160°, *Lwn1* reached a maximum at $\theta_o \sim 30°$. For φ greater than 160°, *Lwn1* decreased at all solar zenith angles, but particularly strongly at larger θ_o. For φ from 0° to 160° there is a little variation, but nothing consistent. In contrast, *Lwn1* at 556.3 nm is fairly stable, until $\varphi = 160°$. Beyond 160°, however, data at 556.3 nm decreased with increasing θ_o. The error bars reflect the standard deviation of the data which went into the average values of each bin.

The structure in *Lwn1* at 444.5 nm, with maximum values at $\theta_o \sim 30°$ needs to be explained. The explanation can come from how MOBY data were collected. In general, MOBY collects data three times a day, at fixed times not fixed θ_o. Given fixed data collection times, θ_o for a given measurement time will vary seasonally, so the variation with θ_o in the data set also reflects a seasonal variation in water properties at the MOBY site. This is evident from a plot of *Chl*, binned in the same manner as the *Lwn1* measurements above, as shown in Fig. 6.

Figure 6 shows that, for a given azimuth range, the chlorophyll is higher at large θ_o (winter months in Hawaii) than in the summer. Because *Lwn1* in the blue decreases with increasing *Chl*, there will be an inverse relationship between how *Chl* and *Lwn1* varies with θ_o in the data set. The *Chl* is also highest for φ between 40° and 50° degrees, which is also where the *Lwn1* is lowest.
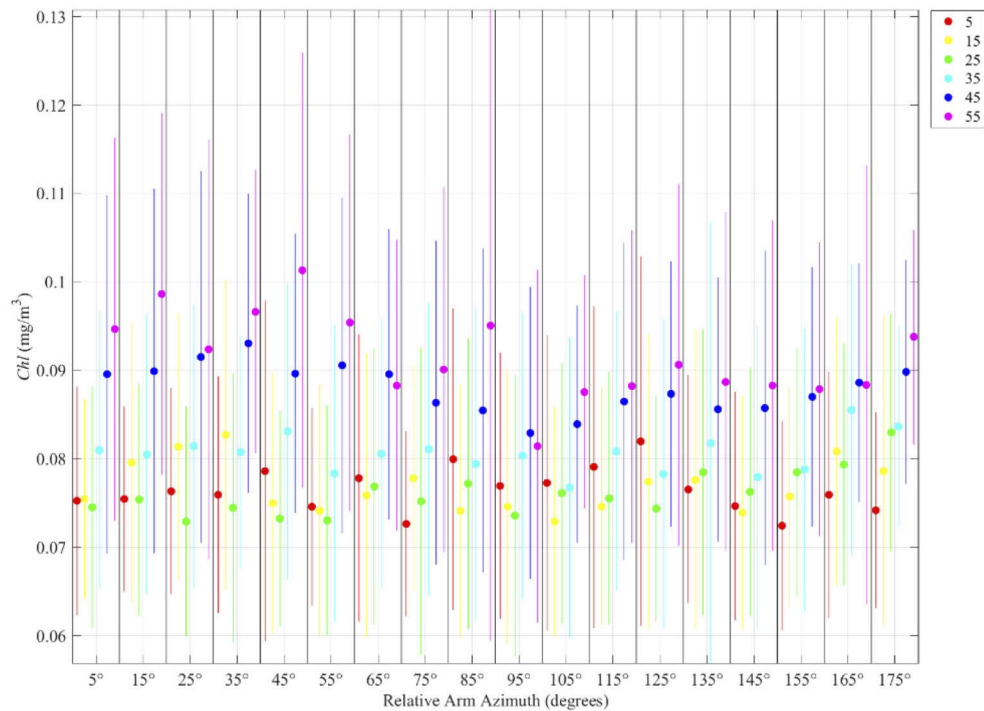
Fig. 6. *Chl* binned by both solar zenith and relative azimuth angles (θ_o and φ). This graph shows a θ_o dependence on *Chl*, caused by the seasonal variation of θ_o. during our measurement times. There is also a small φ dependence, which, since this is random throughout the year, is caused by small statistical variability in the data set. On the x-axis, the label represents the center of the $10°$ bin.

Days for which there were two or more good (cloud free) measurements on the same day provide a check on this interpretation. For each of the days in the MOBY dataset for which there were two or more good measurements, we normalized the BRDF corrected measurement of *Lwn1* at the higher θ_o by the BRDF corrected measurement of *Lwn1* for the measurement at the smallest θ_o for that day. Assuming the water properties did not change significantly and consistently during a single day between these two measurements, one would expect that, on average, there should be no difference in the corrected *Lwn1* during that day. Figure 7 shows the result of this comparison. A linear best fit of the unitless ratio of normalized *Lwn1* pairs to the relative solar zenith angle of the measurements in each pair had a slope not significantly different from 1. Note the colors of the dots represent the smaller θ_o of the pair.

Applying the shadow correction to the data resulted in Fig. 8. As can be seen, for both wavelengths there are two places that the shadow correction visibly effects the data. First for φ greater than $160°$, the correction makes the data much more consistent with the other azimuths. The other place is at very small θ_o, less than $10°$, S'(θ_o, φ, W) brings up the data to create a more consistent trend with the measurements at $\theta_o > 10°$.
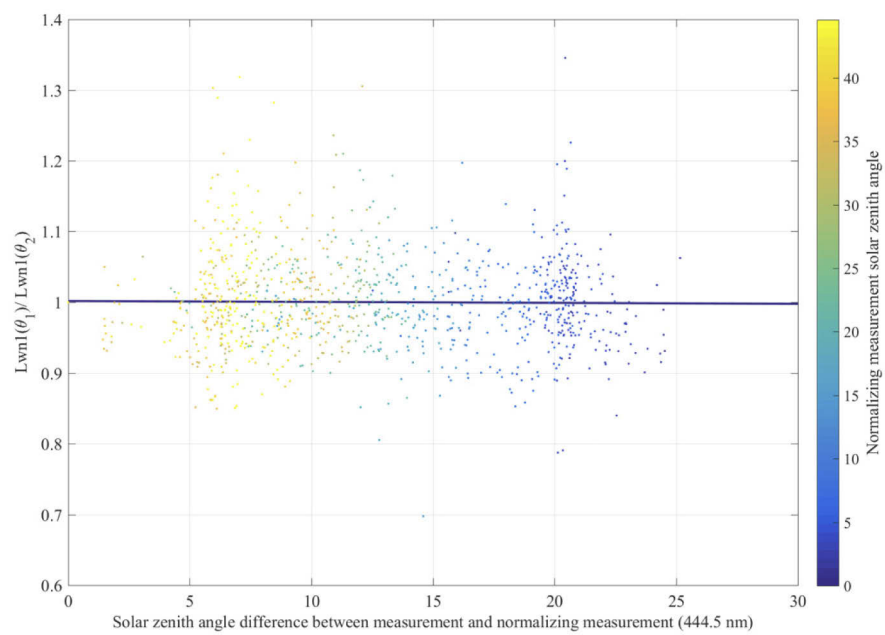
Fig. 7. *Lwn1* pairs normalized by *Lwn1* on the specific day at the lowest θ_o for 444.5 nm. The *x* axis is the difference in θ_o. between the measurements in each pair. The y axis is the unitless ratio of the two *Lwn1* measurements. There is a bold line, nearly along 1, which is the best fit to the data and is not distinguishable from 1.
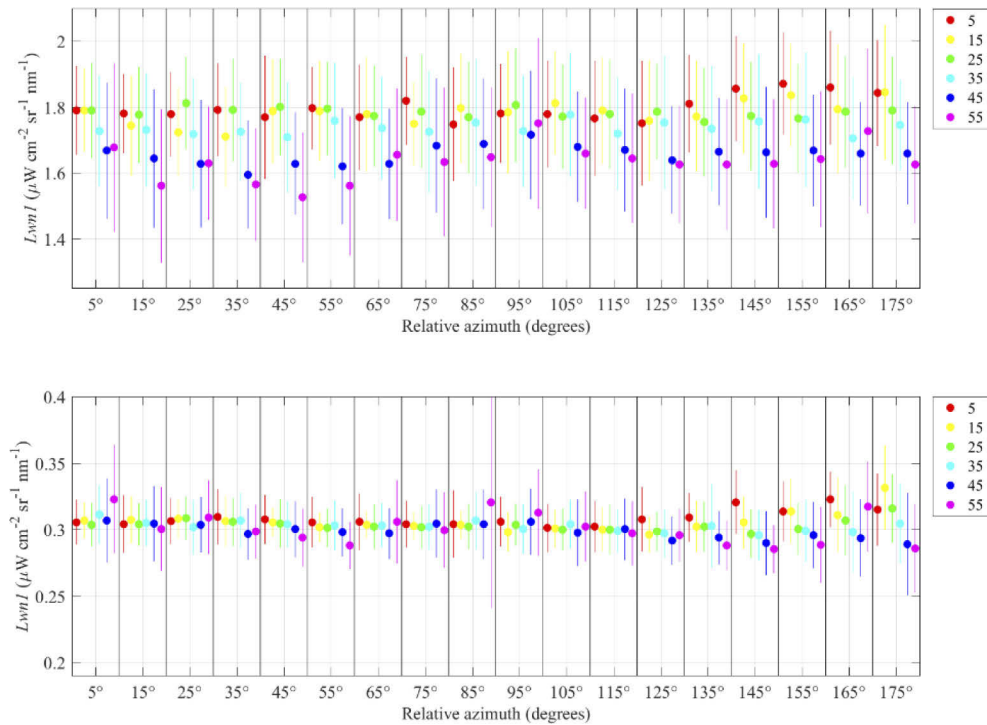
Fig. 8. MOBY time series of *Lwn1*, binned as a function of θ_o and φ after correction for the BRDF effect according to MAG2002BRDF and shadow correction using the $S'(\theta_o, \varphi, W)$ as described. Top graph is 444.5 nm and bottom graph is 556.3 nm. On the x-axis, the label represents the center of the 10° bin.

4. Correction uncertainty

Uncertainty in the correction could have been introduced by residual statistical error in the Monte-Carlo simulation, misrepresenting the effect of the rough surface, errors in the water property model used as input to the Monte-Carlo model, or a misrepresentation of the MOBY structure. The residual statistical error in the Monte-Carlo simulation was determined by investigating the 10 groups of 200 individual runs of 10^8 photons, and then determining the standard deviation of these groups. The coefficient of variation of these groups was very small, less than 0.1% for all wavelengths, indicating that the residual error due to this factor was negligible.

To determine the uncertainty due to the rough surface, it is useful to see the effect of introducing the rough surface on the shadowing correction. Figure 9(A) shows the difference at 440 nm between $S'(\theta_o, \varphi, W)$ with, and without, the wavy surface.

The main impact of the rough surface is in the area near $\varphi = 180°$ (MOBY main buoy between sun and collector). Here the effective spreading of the input solar beam, due to refraction from the rough surface, blurred the shadow and reduced $S'(\theta_o, \varphi, W)$. Also note that the spreading caused a decrease in the shadowing factor at very small azimuth angles, but then caused a small increase in the shadowing factor for many other geometries, as the tilt of the surface moved the light beam into an increased shadow area rather than a decreased shadow area.

The rough surface calculation used the single value of 5 m/s. We also calculated the $S'(\theta_o, \varphi, W)$ for windspeeds of 1 m/s and 10 m/s (neglecting whitecaps at this higher windspeed). The historical windspeed data from the site during measurement times is 5 m/s with a standard deviation of 3.67 m/s, but is not distributed normally. We used our three values of $S'(\theta_o, \varphi, W)$,
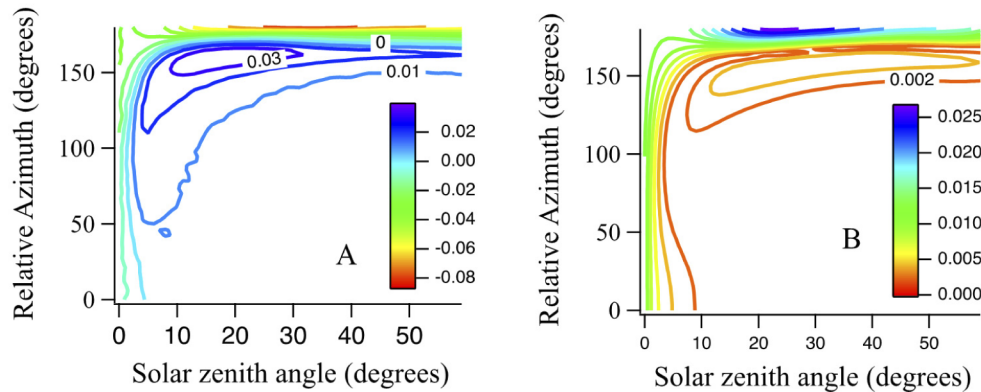
Fig. 9. A: difference between $S'(\theta_o, \varphi, 5\ m/s)$ for rough surface minus flat surface at 440 nm. B: uncertainty in shadow factor at 440 nm caused by using a constant W=5 m/s, based on the histogram of historical windspeed data at MOBY.

and the distribution of windspeeds from the historical data as a weight to calculate the standard deviation of $S'(\theta_o, \varphi, W)$ at each θ_o and φ, using a linear fit to the three values at 1 m/s, 5 m/s, and 10 m/s and the specific θ_o and φ. The uncertainty in $S'(\theta_o, \varphi, W)$, compared with using the one value of 5 m/s is shown in in Fig. 9(B) for 440 nm. Other than near $\varphi = 180°$, the uncertainty due to this factor is very small (< 0.005).

A larger source of uncertainty may be due to possible errors in the water property model IOP's used as input. The important required IOP's were absorption and scattering (a, b respectively), absorption and scattering of pure water (a_w, b_w respectively), and the phase function of the water and particles. The water a_w, b_w, and water phase function are relatively well known [17,18]. Our model runs used a single *Chl* value to determine a and b through the Morel and Maritorena model [21]. As seen earlier, the range of *Chl* seen at the MOBY site is small. To determine the uncertainty caused by using this one value of *Chl*, we ran the shadow correction for water properties corresponding to *Chl* equal to 0.05 mg/m³, 0.1 mg/m³, and 0.15 mg/m³. For each θ_o and φ, we calculated a linear fit to the three values of $S'(\theta_o, \varphi, W)$ at that θ_o and φ and Log(*chl*). The distribution of *Chl* values at the MOBY site was obtained by using the CI -Chlorophyll algorithm [20], with the MOBY hyperspectral data. A gaussian distribution of 10^4 values of *Chl* with a mean of 0.08 mg/m³ and a standard deviation of 0.007 mg/m³, reflecting the time series of values at the MOBY site, was used with a linear fit of $S'(\theta_o, \varphi, W)$ calculated for the three values of Log(*Chl)* at each θ_o and φ to get 10^4 values of $S'(\theta_o, \varphi, W)$, from which the standard deviation was calculated. The resulting uncertainty for 444.5 nm is shown in Fig. 10(A). As can be seen, for the distribution of Chl seen at the site, the standard deviation of $S'(\theta_o, \varphi, W)$ due to this variation was small. The total difference in $S'(\theta_o, \varphi, W)$ between *Chl* = 0.05 mg/m³ and *Chl*=0.15 mg/m³, was only 3.0% in the region where the shadowing correction is 19%.

The other IOP needed for the calculation was the particle phase function. The program used a Fournier-Forand phase function, which was characterized by the b_b/b ratio. For the calculations used here, we used the classic value from Petzold [22] of 0.0183. The full range of b_b/b for clear surface waters is probably 0.005 to 0.03 [31,32]. We ran the case of 0.005 and 0.05, going to the extreme high end, with 5% backscattering, to see the variation that this might cause in the results. At both 440 nm and 560 nm, in the region of maximum shadow (at $\varphi = 180°$, $\theta_o = 30°$), $S'(\theta_o, \varphi, W)$ calculated was different by 30% (a 6% difference in the final shadow corrected value of *Lwn1*), however at $\varphi <150°$ the difference was less than 1% in the final shadow corrected value for *Lwn1*. To characterize the uncertainty we used three values of $S'(\theta_o, \varphi, W)$ calculated with b_b/b of 0.005, 0.0183, and 0.05, and again did a linear fit of the $S'(\theta_o, \varphi, W)$ vs log(b_b/b) for each
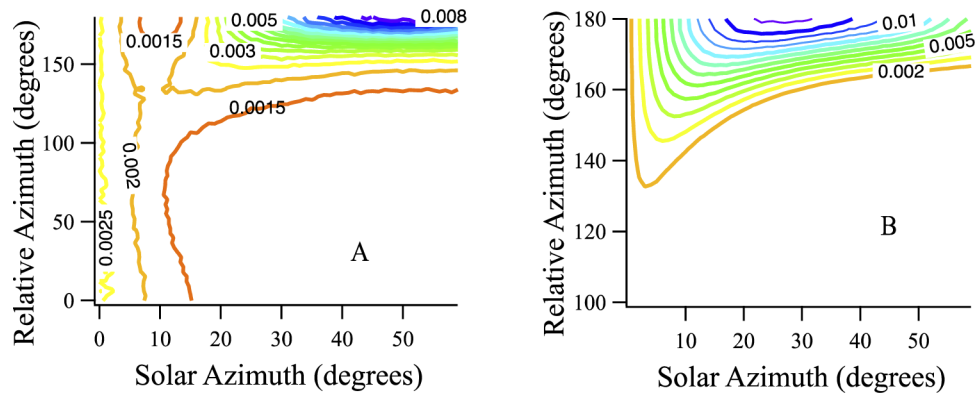
Fig. 10. A: Uncertainty for $S'(\theta_o, \varphi, W)$ due to a single value of $Chl = 0.1$ mg/m^3 at 443 nm. B: Uncertainty for $S'(\theta_o, \varphi, W)$ due to a single value of $b_b/b = 0.0183$ at 443 nm.

θ_o and φ. The GUM (Guide to the Expression of Uncertainty in Measurement) [33] indicates that if a parameter is equally probable within a given range, $\pm a$, then the uncertainty is $a/\sqrt{3}$. We estimate that realistically, in this clear water, b_b/b was within the range of 0.005 and 0.03. We used a distribution of 10^4 values of b_b/b with a mean of 0.0183 and standard deviation of 0.012 (twice the GUM value), and generated $S'(\theta_o, \varphi, W)$ at each b_b/b using the fit parameters. From this, a standard deviation of the 10^4 values can be determined, and this was used to characterize the uncertainty. The resulting uncertainty is shown in Fig. 10(B) for 443 nm. This can be seen to be quite small, except in the region of highest shadowing factor.

These 4 sources of uncertainty can be combined either by a summation, or through a root-sum-squares (RSS) calculation. The last factor, the uncertainty due to not handling the structure properly, can only be determined by looking at the final results effect on the MOBY data set, and determining how well the corrected data are independent of φ. This is made more difficult by the variation in water properties inside each bin. The total uncertainty, using the summation of the factors as described is shown in Fig. 11 for 440 nm.
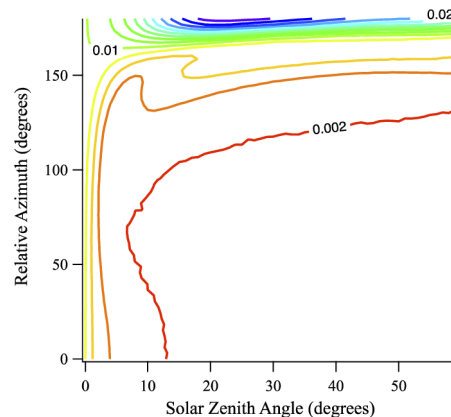

Fig. 11. Total uncertainty, k=1, for $S'(\theta_o, \varphi, W)$ at 440 nm.

The shadowing correction does not include inelastic scattering, which is important at wavelengths near 550 nm and above [27,28]. Inelastic scattering will negate, to some extent, the effect of high absorption on shadowing at these longer wavelengths. This is because the excitation is in
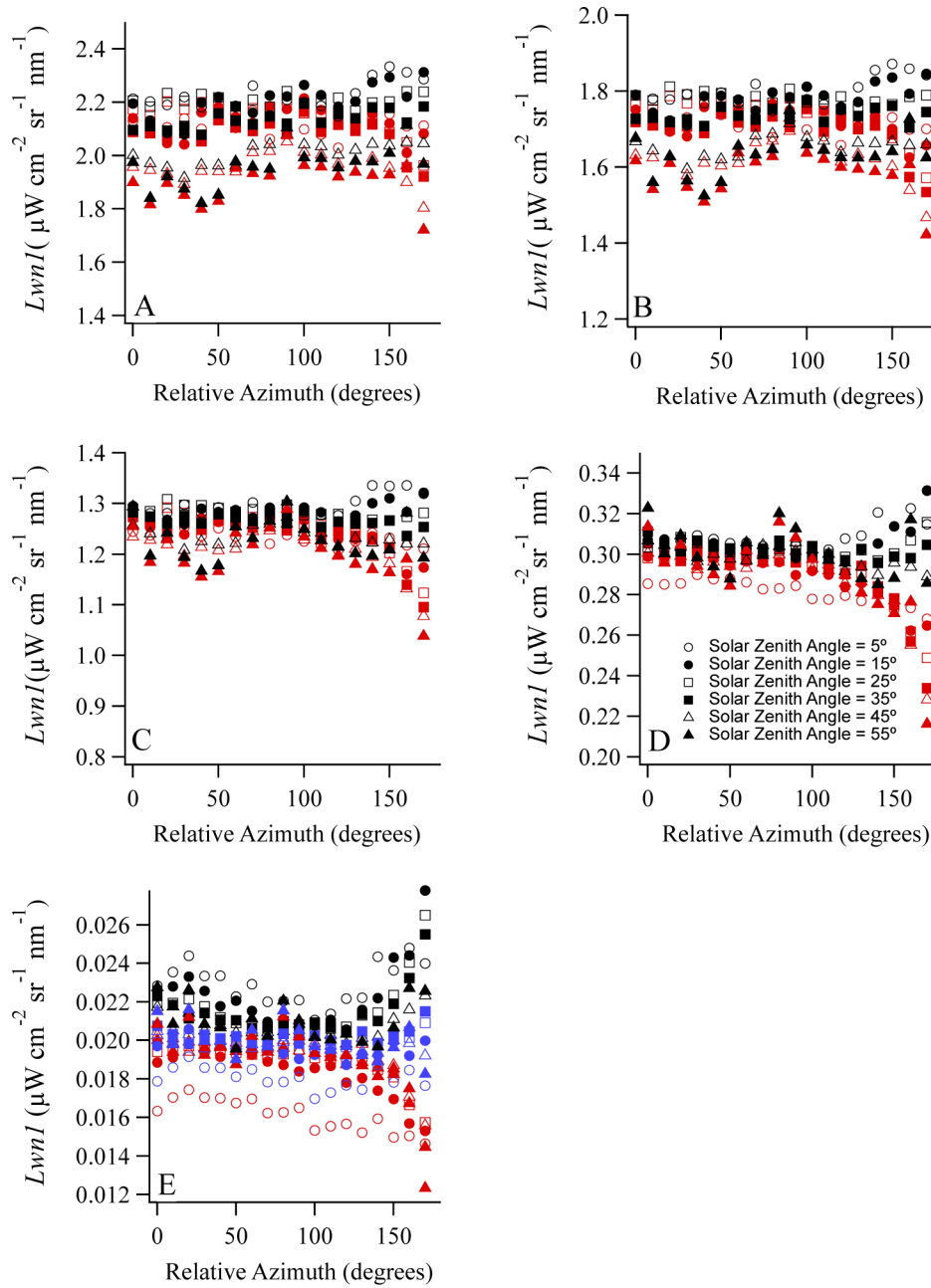
Fig. 12. Corrected (black) and uncorrected (red) *Lwn1* data for the VIIRS visible ocean color bands: A) 412.9 nm, B) 444.5 nm, C) 481.2 nm, D) 556.3 nm, and E) 674.6 nm. Different solar zenith angles are presented as different symbols, as displayed in the legend in panel D. The blue symbols in (E) are an alternate correction, which uses the correction at 575 nm for all wavelengths above this value. Grey shading in Figs. A-D is the estimated uncertainty in the corrected values, in Fig. E the blue shading is the estimated uncertainty in the alternate correction.

the blue, which has a lower absorption and thus less shadowing. An alternate correction, used $S'(\theta_o, \varphi, W)$ for 575 nm for all wavelengths above this wavelength. This is shown as the blue symbols in Fig. 12(E). This significantly reduced what appeared to be the over correction for shadowing.

5. Conclusions

Figure 12 shows the corrected vs uncorrected data for 5 wavelengths, corresponding to the visible VIIRS ocean color bands. These data were binned in the same manner as Figs. 4, 5, 6, and 8. The red shaded symbols are before correction, the black are after correction for shadowing. For 412.9 nm and 444.5 nm, it was difficult to see the trend, because these are very sensitive to variations in chlorophyll, which, due to sampling, varied slightly between points. At 481.2 nm and longer wavelengths, before the shadow correction, there was an obvious decrease towards the highest φ which the shadow correction flattens out. For 556.3 and 674.6 nm, there appeared to be a small over correction. As has been seen, the biggest shadowing was generally at θ_o of 35° to 55°, and $\varphi > 150°$. For 556.3 nm and 674.6 nm, there was also an effect at very small θ_o (sun directly overhead). This also looks like it has been overcorrected, particularly at 674 nm. But this is a difficult region to correct, as it depends on the effect of a relatively small shadow (the arm and collector).

The analysis shown above included an estimate of the uncertainty, which can be applied to each measurement based on the specific geometry and wavelength of that measurement. The uncertainty was displayed in Fig, 12 as the shaded area. The uncertainty was largest at high φ, and very small elsewhere. For the most part, the uncertainty was only 30% of the correction at the highest φ, so a 3% effect on the final *Lwn1*. At other φ the uncertainty was very small, much less than 1% of the final *Lwn1*.

This 3-D correction is between 50% and 100% larger than the earlier 2-D correction [6]. The 2-D correction was based on at least two factors that might account for this. First, the 3-D correction is done at higher spatial and angular resolution (3° azimuthal resolution vs 15° for the 2-D model). Second, when investigating which part of the structure is causing the shadow, it is obvious, from the geometry, that in the 3-D model, the surface buoy's vertical structure causes much more shadowing that is not captured in the 2-D model.

This correction will be made available for the MOBY water leaving radiance data set, along with the uncertainty in the correction. As discussed, for azimuths less than 150°, the correction is small. In general, for azimuthal angles greater than 150°, the uncertainty of the correction was less than 20% of the correction. We are working towards determining a measurement by measurement wavelength dependent uncertainty for the entire MOBY data set, which will include this shadowing factor.

Disclosures. The authors declare no conflicts of interest.

Data availability. The entire MOBY data set, used for validation in this study, is available at Ref. [34]. The shadowing correction will be made available at this site, along with the uncertainty for this correction.

References

1. H. R. Gordon and K. Ding, "Self-shading of in-water optical instruments," Limnol. Oceanogr. **37**(3), 491–500 (1992).
2. J. Piskozub, "Effect of 3-D instrument casing shape on self-shading of in-water upwelling irradiance," Opt. Express **12**(14), 3144–3148 (2004).
3. R. A. Leathers, T. V. Downes, and C. D. Mobley, "Self-shading correction for upwelling sea-surface radiance measurements made with buoyed instruments," Opt. Express **8**(10), 561–570 (2001).
4. J. P. Doyle and G. Zibordi, "Optical propagation within a three dimensional shadowed atmosphere ocean field: application to large deployment structures," Appl. Opt. **41**(21), 4283–4306 (2002).
5. J. Piskozub, A. R. Weeks, J. N. Schwarz, and I. S. Robinson, "Self-shading of upwelling irradiance for an instrument with sensors on a sidearm," Appl. Opt. **39**(12), 1872–1878 (2000).

6. J. L. Mueller, "Shadow Corrections to In-water upwelled radiance measurements: A status Review," *Chapter 6 in Ocean Optics Protocols for Satellite Ocean Color Sensor Validation, Revision 5, Volume VI, Part 2: Special topics in Ocean Optics Protocols*. J. L. Mueller and G. S. Fargion, eds. NASA Goddard Space Flight Center, Greenbelt, MD. NASA/TM-2004:1-7 (2004).

7. E. Leymarie, C. Penkerc'h, V. Vellucci, C. Lerebourg, D. Antoine, E. Boss, M. R. Lewis, F. D'Ortenzio, and H. Claustre, "ProVal: A new autonomous profiling float for high quality radiometric measurements," Front. Mar. Sci. **5**, 437 (2018).

8. A. Bialek, V. Vellucci, B. Gentili, D. Antoine, J. Gorrono, N. Fox, and C. Underwood, "Monte Carlo-based quantification of uncertainties in determining ocean remote sensing reflectance from underwater fixed-depth radiometry measurements," J. Atm. and Ocean. Tech. **37**(2), 177–196 (2020).

9. G. P. Gerbi, E. Boss, P. J. Werdell, C. W. Proctor, N. Haentjens, M. L. Lewis, K. Brown, D. Sorrentino, J. R. V. Zaneveld, A. H. Barnard, J. Koegler, H. Fargher, M. DeDonato, and W. Wallace, "Validation of ocean color remote sensing reflectance using autonomous floats," J. Atm. and Ocean. Tech. **33**(11), 2331–2352 (2016).

10. D. K. Clark, H. R. Gordon, K. J. Voss, Y. Ge, W. Broenkow, and C. C. Trees, "Validation of atmospheric corrections over oceans," J. Geophs. Res. **102**(D14), 17209–17217 (1997).

11. D. K. Clark, M. A. Yarbrough, M. E. Feinholz, S. Flora, W. Broenkow, Y. S. Kim, B. C. Johnson, S. W. Brown, M. Yuen, and J. L. Mueller, "MOBY, a radiometric buoy for performance monitoring and vicarious calibration of satellite ocean color sensors: Measurement and data analysis protocols," *Ocean Optics Protocols for Satellite Ocean Color Sensor Validation, Revision 3*, Volume 2. J. L. Mueller and G. S. Fargion, eds., NASA Goddard Space Flight Center, Greenbelt, MD. NASA/TM–2002-21004:138-170 (2002)

12. R. A. Barnes, R.E. Eplee Jr., G.M. Schmidt, F.S. Patt, and C.R. McClain, "The calibration of SeaWiFS, part1: Direct techniques," Appl. Opt., **40** (36), 6682–6700 (2001)

13. R. E. Eplee Jr., W. D. Robinson, S. W. Bailey, D. K. Clark, P. J. Werdell, M. Wang, R. A. Barnes, and C. R. McClain, "The calibration of SeaWiFS, part 2: Vicarious techniques," Appl. Opt., **40**(36), 6701–6718 (2001).

14. M. Wang, W. Shi, L. Jiang, and K. Voss, "NIR- and SWIR-based on-orbit vicarious calibrations for satellite ocean color sensors," Opt. Express **24**(18), 20437–20453 (2016).

15. A. W. Harrison, "Directional sky luminance versus cloud cover and solar position," Sol. Energy **46**(1), 13–19 (1991).

16. W. W. Gregg and K. L. Carder, "A simple spectral solar irradiance model for cloudless maritime atmospheres," Limnol. and Oceanogr. **35**(8), 1657–1675 (1990).

17. R. M. Pope and E. S. Fry, "Absorption spectrum (380-00 nm) of pure water. II. Integrating cavity measurements," Appl. Opt. **36**(33), 8710–8723 (1997).

18. A . Morel, "Optical Properties of Pure Water and Pure Sea Water," *Optical Aspects of Oceanography*, N. G. Jerlov and E. S. Nielsen eds., Academic, New York, 1974, chap . 1, pp 1–24.

19. G. Fournier and J. L. Forand, "Analytic phase function for ocean water," *In Ocean Optics XII,* SPIE2258, J. S. Jaffe, ed., 194–201 (1994).

20. C. Hu, Z. Lee, and B. Franz, "Chlorophyll a algorithms for oligotrophic oceans: A novel approach based on three-band reflectance difference," J. Geophys. Res., **117**(C1), C01011 (2012).

21. A. Morel and S. Maritorena, "Bio-optical properties of oceanic waters: a reappraisal," J. Geophys. Res.-Oceans **106**(C4), 7163–7180 (2001).

22. T. J. Petzold, "Volume scattering functions for selected ocean waters," Scripps Institution of Oceanography Report SIO 72-78, 79 (1972).

23. G. Thuillier, M. Hersé, D. Labs, T. Foujols, W. Pettermans, D. Gillotay, P. C. Simon, and H. Mandel, "The Solar Spectral Irradiance from 200 to 2400 *nm* as Measured by the SOLSPEC Spectrometer from the Atlas and Eureca Missions," Sol. Phys. **214**(1), 1–22 (2003).

24. H. R. Gordon, "Physical principles of Ocean Color Remote Sensing," DOI: 10/333596/ppocrs-19 (2019).

25. C. Cox and W. Munk, "Measurement of the Roughness of the Sea Surface from Photographs of the Sun's Glitter," J. Opt. Soc. Am. **44**(11), 838–850 (1954).

26. M. D. Goldberg, H. Kilcoyne, H. Cikanek, and A. Mehta, "Joint Polar Satellite System: The United States next generation civilian polar-orbiting environmental satellite system," J. Geophys. Res.: Atmos. **118**(24), 13,463–13,475 (2013).

27. H. Gordon, "Contribution of Raman scattering to water-leaving radiance: a reexamination," Appl. Opt. **38**(15), 3166–3174 (1999).

28. K. J. Voss, H. R. Gordon, S. Flora, B. C. Johnson, M. Yarbrough, M. Feinholz, and T. Houlihan, "A method to extrapolate the diffuse upwelling radiance attenuation coefficient to the surface as applied to the Marine Optical Buoy (MOBY)," J. Atm. and Ocean. Tech. **34**(7), 1423–1432 (2017).

29. A. Morel and B. Gentili, "Diffuse reflectance of oceanic waters: its dependence on Sun angle as influenced by the molecular scattering contribution," Appl. Opt. **30**(30), 4427–4438 (1991).

30. A. Morel, D. Antoine, and B. Gentili, "Bidirectional reflectance of oceanic waters: accounting for Raman emission and varying particle scattering phase function," Appl. Opt. **41**(30), 6289–6306 (2002).

31. M. S. Twardowski, E. Boss, J. B. Macdonald, W. S. Pegau, A. H. Barnard, and J. R. V. Zaneveld, "A model for estimating bulk refractive index from the optical backscattering ratio and the implications for understanding particle composition in case I and case II waters," J. Geophys. Res. **106**(C7), 14129–14142 (2001).

32. A. L. Whitmire, E. Boss, T. J. Cowles, and W. S. Pegau, "Spectral variability of the particulate backscattering ratio," Opt. Express **15**(11), 7019–7031 (2007).
33. Working Group 1 of the Joint Committee for Guides in Metrology, "Evaluation of measurement data – Guide to the expression of uncertainty in measurement," BIPM, JCGM 100:2008, (2008).
34. https://coastwatch.noaa.gov/cw/field-observations/MOBY.html